Research Square

Preprints are preliminary reports that have not undergone peer review.
They should not be considered conclusive, used to inform clinical practice,
or referenced by the media as validated information.

A computer-aided manufacturing tool for analyzing the tool-workpiece contact during the micro grinding of dental prostheses

Nicolas LEBON

nicolas.lebon@devinci.fr

DVRC: De Vinci Research Center https://orcid.org/0000-0002-4377-9849

Laurent TAPIE

Research Article

Keywords: Dental CAD/CAM, micro-grinding, prosthesis, machining, grinding speed, tool-workpiece contact

Posted Date: June 29th, 2026

DOI: https://doi.org/10.21203/rs.3.rs-9860168/v1

License: This work is licensed under a Creative Commons Attribution 4.0 International License.
Read Full License

Version of Record: A version of this preprint was published at The International Journal of Advanced Manufacturing Technology on October 5th, 2026. See the published version at https://doi.org/10.1007/s00170-026-19204-0.

A computer-aided manufacturing tool for analyzing the tool-workpiece contact during the micro grinding of dental prostheses

Nicolas LEBON *[a,b] (Assistant professor in Mechanical Engineering),

ORCID : 0000-0002-4377-9849

Laurent TAPIE [c] (Associate professor in Mechanical Engineering),

ORCID : 0000-0002-6857-441X

a. De Vinci Higher Education, De Vinci Research Center, Paris, France nicolas.lebon@devinci.fr

b. Université Paris Cité and Sorbonne Paris Nord, Inserm, Santé Orale, F-92120 Montrouge, France

c. Université Sorbonne Paris Nord and Paris Cité, Inserm, Santé Orale, F-92120 Montrouge, France

*Correspondence to: Nicolas LEBON, Pôle Léonard de Vinci, 41 allée Le Corbusier 92000 Nanterre.

Email: nicolas.lebon@devinci.fr; Tel: +33 1 81 00 28 36

Abstract

Dental CAD/CAM manufacturing predominantly relies on three-axis milling strategies, which impose geometric and kinematic constraints that influence machining conditions and prosthesis quality. This study investigates tool–workpiece contact configurations and effective grinding speed variations during the micro-grinding of dental prostheses. Two abrasive burs were geometrically characterized and modeled using an APT-based analytical formalism. The resulting models enabled the determination of local contact conditions and effective grinding speeds on freeform crown geometries.

The methodology was implemented on a clinical dental crown model to evaluate the spatial distribution of tool engagement, grinding speed, and machining accessibility. Results showed that, regardless of tool geometry, machining is performed almost exclusively by the hemispherical tip of the bur, while conical and cylindrical sections contribute marginally. Consequently, effective grinding speed exhibits strong spatial variability driven mainly by local surface orientation. The lowest speeds occur at cusp tips, whereas higher values are observed along peripheral regions, suggesting significant variations in surface integrity, roughness, and tool wear across the prosthesis.

A curvature-based accessibility analysis revealed that 40,1% of the crown surface is inaccessible under three-axis machining constraints, particularly within anatomically important grooves and fossae. Because these regions contribute to food guidance, fragmentation, and occlusal contact distribution during mastication, their incomplete reproduction may compromise the functional anatomy of the restoration and reduce masticatory efficiency.

These findings demonstrate the strong coupling between prosthesis geometry, tool design, and machining kinematics, highlighting the need for advanced manufacturing strategies, such as multi-axis machining, to improve accessibility, preserve functional morphology, and enhance prosthesis performance.

Keywords: Dental CAD/CAM, micro-grinding, prosthesis, machining, grinding speed, tool-workpiece contact.

1. Introduction

Dental prostheses manufacturing has undergone a significant transformation over the past two decades, largely driven by the rapid development of computer-aided design and computer-aided manufacturing (CAD/CAM) technologies. These systems enable the fabrication of highly customized ceramic prosthetic restorations with complex freeform geometries, either chairside or

in laboratory environments [1]. The integration of digital workflows, from intraoral scanning to computer-aided manufacturing, has improved reproducibility, reduced production time, and expanded geometric possibilities.

Despite these advances, most dental CAD/CAM systems rely on parallel plane milling strategies associated with micro-grinding of brittle ceramics, in which toolpaths are generated on the mesh of the prosthesis CAD model along predefined guide planes [2-4]. While robust and economically efficient, this manufacturing configuration imposes inherent geometric and kinematic constraints. In particular, machining freeform dental geometries with a fixed tool orientation leads to highly variable local grinding conditions [5].

The complex morphology of dental prostheses induces continuous variations in the position of the contact point between the grinding tool and the workpiece. Because the effective grinding speed depends on the local effective grinding radius, which itself varies with the relative orientation between the tool axis and the surface normal. Substantial fluctuations in grinding speed occur during machining. Consequently, the actual grinding conditions may significantly deviate from the nominal programmed parameters.

These variations directly affect both tool behavior and surface integrity [6-9]. From the tool perspective, changes in effective grinding speed influence wear mechanisms, wear localization, and overall tool life [10-12]. From the prosthesis perspective, surface integrity, including roughness, residual stresses, and potential subsurface damage, is strongly dependent on grinding speed and tool wear, both of which are governed by local tool–surface orientation [13,14].

In addition to grinding speed variability, geometric accessibility constitutes another critical limitation of three-axis machining [15, 16]. Certain regions of the prosthesis may become partially or fully inaccessible due to curvature constraints and tool geometry. These non-machinable areas can compromise dimensional accuracy and surface quality, particularly in highly concave zones.

The objective of this study is to analyze the tool–prosthesis contact conditions during three-axis milling of dental restorations. First, two geometric models describing the tool tip and the local contact configuration between the milling tool and the prosthetic surface are developed, enabling the determination of the effective grinding speed at any point on the surface. Then, the proposed models are implemented to analyze the tool contact on a crown shape to evaluate their practical relevance to help dental CAD/CAM manufacturers in developing new machining strategies.

2. Tool/prosthesis contact geometrical modeling

Dental CAD/CAM machines typically operate using highly simplified machining sequences. In most clinical workflows, a single finishing operation is directly applied to the prosthetic geometry,

without prior roughing strategies. Consequently, the final prosthetic shape is obtained directly from this finishing stage.

In three-axis machining, the milling of complex prosthetic geometries induces significant variations in the relative orientation between the tool and the workpiece. Assessing the impact of these variations on surface integrity and tool wear requires a comprehensive geometric modeling of the abrasive burs used in dental CAD/CAM systems, together with a description of the tool–prosthesis contact and the associated effective grinding speed.

2.1 Grinding bur model

Two commercially available abrasive burs commonly used in dental CAD/CAM systems were selected for this study. The first tool, designated PrograMill Tool Red Ø1.0, is supplied with the Ivoclar PrograMill PM7 labside milling machine. The second tool, referred to as Cerec Cylinder Pointed Bur 12S, is marketed by Dentsply Sirona and is compatible with the Cerec MCXL chairside and labside systems.

Both tools were geometrically characterized using optical microscopy (Keyence VHX-8000), enabling precise measurement of their active tip geometry. The main geometric parameters obtained from these measurements are summarized in Table 1.

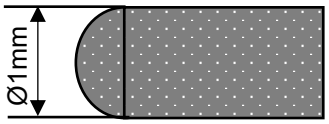
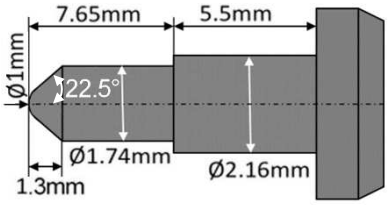
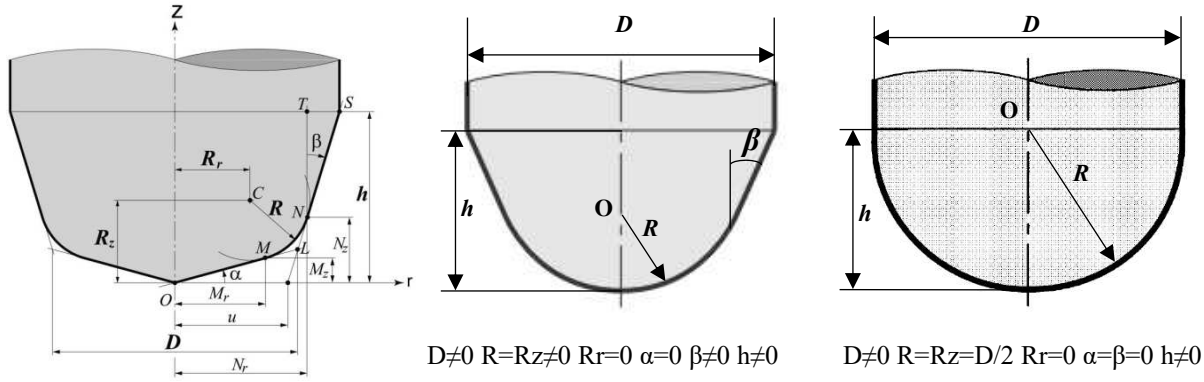
Tool			Geometry	Code
Ball end mill	PrograMill Tool Red g1.0 for PM7 [17]. Ivoclar, Schaan, Liechtenstein			PM
Tapper ball end mill	Cerec cylinder pointed bur 12S [17]. Sirona Dental Systems GmbH, Bensheim, Germany.			CER

Table 1: Tools with their geometries and codes included in the study.

The tip geometries of the two tools are globally comparable. Both burs exhibit a hemispherical end geometry with a nominal tip radius of 1 mm. Differences arise in the cylindrical shank region. The active cylindrical diameter is 1.74 mm for the CER tool and 1.00 mm for the PM tool. Although the CER tool presents a maximum diameter of 2.16 mm, this portion does not participate in the milling process and therefore does not contribute to the effective grinding geometry.

The APT system defines the geometric envelope of a milling tool using seven parameters (D, R, R_r, R_z, α, β, and h) (Fig. 1) [17]. Originally developed for conventional cutting tools, this parametric description is adopted in the present study and adapted to model the geometry of abrasive burs used in dental CAD/CAM applications. This transposition enables a consistent and analytical representation of the tool envelope, suitable for subsequent contact analyses.



a) Generalized geometric APT modeling

b) Tapper ball end mill modeling (CER)

c) Ball end mill modeling (PM)

Fig. 1: APT geometrical modeling [17].

Within the APT formalism, two specific configurations of the hemispherical end mill are defined, allowing the geometries of the two selected burs to be accurately represented (Figs. 1b, 1c). For each tool, only the relevant non-zero geometric parameters are summarized in Table 2.

Tools	PM	CER
APT parameters	D=1 mm R=Rz=0,5 mm β=0° h=1 mm	D=1.74 mm R=Rz=0,5 mm β=22,5° h=1.3 mm

Table 2: APT parameters applied to the tools included in the study.

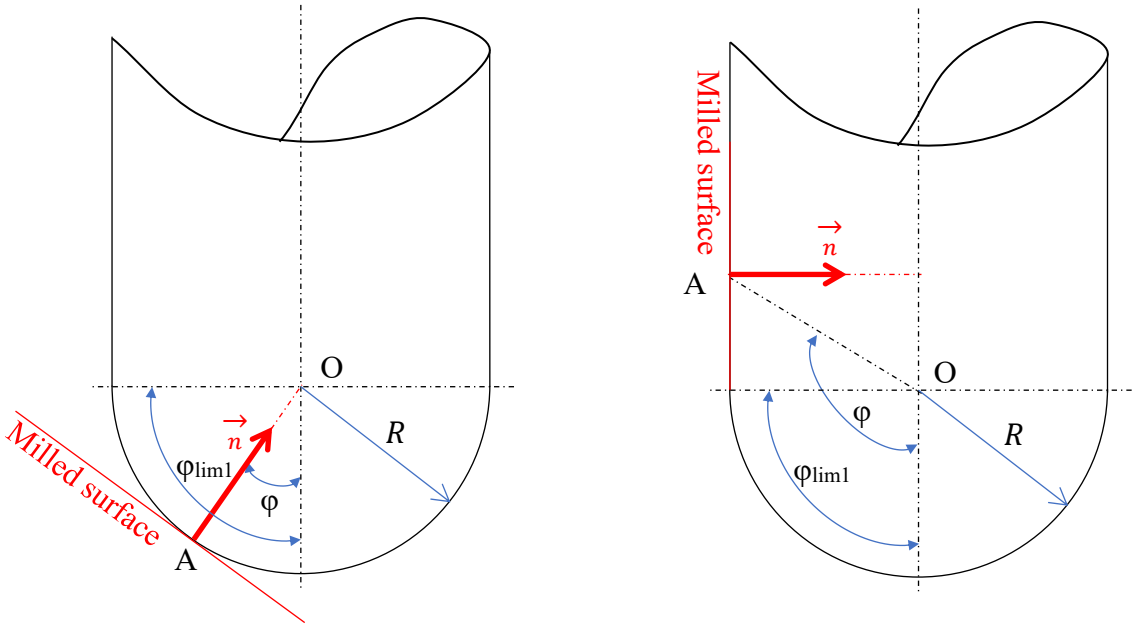
2.2 Contact configuration types

The theoretical contact point between the tool and the machined surface is denoted by A (Figure 2). The center of the hemispherical tip is denoted by O. The angular position between the tool axis and [OA] is defined as φ ∈ [0; 180°[. Accordingly, the position of point A, in a polar coordinate system centered at O, is characterized by the pair $\left(\| \overrightarrow{OA} \|, \varphi\right)$.

2.2.1 PM tool case

Contact point A may lie either on the hemispherical tip or on the cylindrical flank of the tool, depending on the local surface orientation. Consequently, two distinct contact configurations can be identified (Fig. 2). In the first configuration, contact occurs on the hemispherical portion of the

tool. In this case, the angular position satisfies $0 \leq \varphi \leq \varphi_{lim1} = 90°$ (Fig. 4a). In the second configuration, contact takes place on the cylindrical flank. The angular position then ranges from $\varphi_{lim1} = 90°$ to $\varphi_{lim2} = 175°$ (Fig. 4b).



a) Hemispherical part contact configuration
$\varphi_{lim1}=90°$
$0<\varphi<\varphi_{lim1}$

b) Cylindrical part contact configuration
$\varphi_{lim1}=90°$ $\varphi_{lim2}=175°$
$\varphi_{lim1}<\varphi<\varphi_{lim2}$

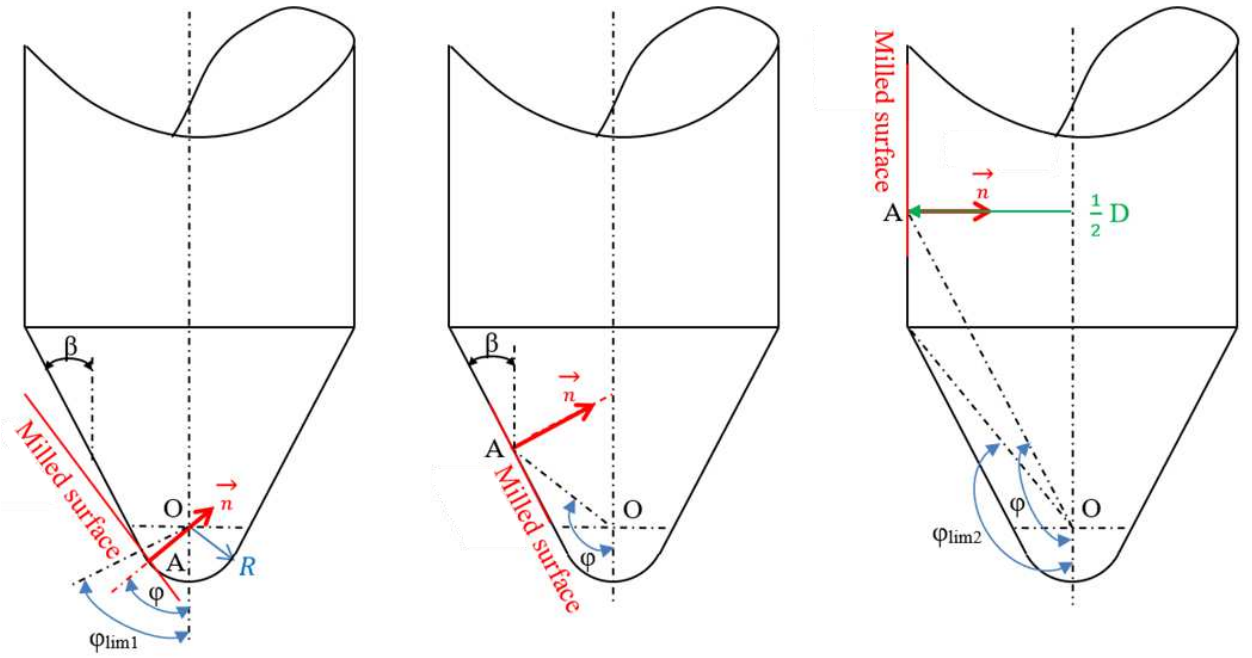
A: tool/prosthesis contact point	O: hemispherical part center
$\vec{n}$: tool/prosthesis normal at the point A	R: hemispherical part radius
φ: contact point angular position	

Fig. 2: PM tool/prothesis contact schematic and parameters.

2.2.2 CER tool case

Contact point A may lie either from the hemispherical tip to the conical section, and finally to the cylindrical flank of the tool, resulting in three distinct contact configurations (Fig. 3).

In the first configuration, contact occurs on the hemispherical tip, with the angular position φ ranging from 0 to $\varphi_{lim1} = 90° - \beta = 67.5°$ (Fig. 5a). In the second configuration, contact occurs on the conical section, with φ ranging from $\varphi_{lim1} = 67.5°$to $\varphi_{lim2} = 132.38°$ (Fig. 5b). Finally, in the third configuration, contact occurs on the cylindrical flank, with φ between $\varphi_{lim2} = 132.38°$and $\varphi_{lim3} = 173°$ (Fig. 5c).



a) Hemispherical part contact configuration
$\varphi_{lim1}=(90°-\beta)=67,5°$
$0<\varphi<\varphi_{lim1}$

b) Conical part contact configuration
$\varphi_{lim1}=(90°-\beta)=67,5°$ $\varphi_{lim2}=132,38°$
$\varphi_{lim1}<\varphi<\varphi_{lim2}$

c) Cylindrical part contact configuration
$\varphi_{lim2}=(90°-\beta)=132,38°$ $\varphi_{lim3}=173°$
$\varphi_{lim2}<\varphi<\varphi_{lim3}$

A: tool/prosthesis contact point	β: clearance angle
$\vec{n}$: tool/prosthesis normal at the point A	φ: contact point angular position
R: hemispherical part radius	D: cylindrical part diameter
O: hemispherical part center	

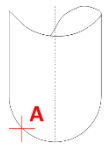
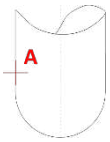
Fig. 3: CER tool/prothesis contact schematic and parameters.

2.3 Effective grinding speed model

Changes in the position of contact point A, during machining, lead to variations in the effective grinding speed (Vc(φ)). Based on previous tool geometry models and geometric modeling of the tool/prosthesis contact, expressions for the effective grinding speed Vc(φ) at contact point A were established. The literal expressions for each contact configuration and tool are given, assuming a known and constant spindle speed (N), as the dental CNC spindles are not fitted with variable speed drives.

2.3.1 PM tool case

Depending on the position of the tool/prosthesis contact point, the effective grinding speed at contact point A takes on different literal expressions (Tab. 3).

Contact configuration		Equation	
 **Hemispheric part**	$0<\varphi<\varphi_{lim1}$ $\varphi_{lim1}=90°$	$Vc(\varphi) = \frac{N * \pi * R * Sin(\varphi)}{500}$	Eq. 1
 **Cylindric part**	$\varphi_{lim1}<\varphi<\varphi_{lim2}$ $\varphi_{lim1}=90°$ $\varphi_{lim2}=175°$	$Vc = \frac{N * \pi * D}{1000} = cte$	Eq. 2
R(mm), φ(deg), β(deg), N(rpm), Vc(m/min)			

Tab. 3: Effective grinding speed equations as a function of contact configuration for the PM tool.

The equations presented in Table 3 can be used to graphically represent the non-linear evolution of the effective grinding speed as a function of the angular position (φ) (Fig. 4). Three spindle speeds currently used in dental milling machines are represented. Since the tool geometry is tangentially continuous, the evolution of $V_c(\varphi)$remains continuous at the tangency point. A marked increase in grinding speed occurs over the hemispherical section of the tool.

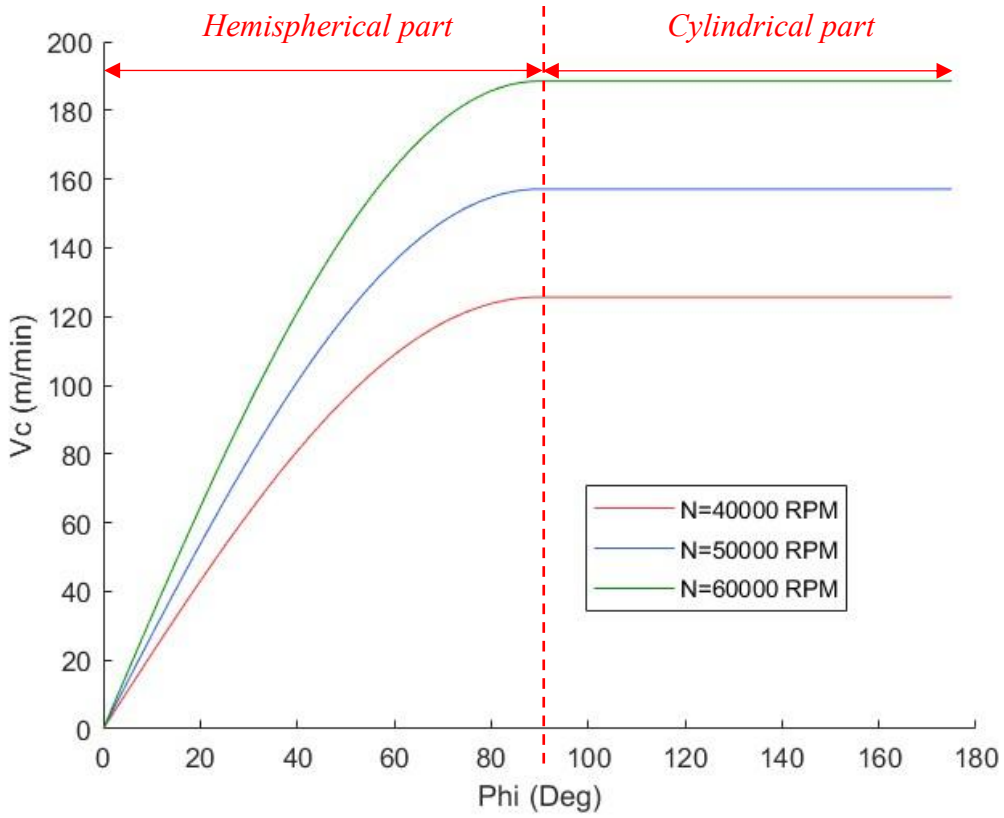
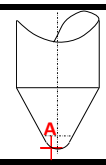
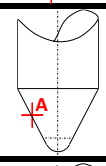
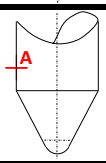


Fig. 4: Vc(φ) trend for the PM bur.

2.3.2 CER tool case

Depending on the position of the tool/prosthesis contact point, the effective grinding speed at contact point A takes on different literal expressions (Tab. 4).

Contact configuration			Equation	
	**Hemispheric part**	$0<\varphi<\varphi_{lim1}$ $\varphi_{lim1}=(90°-\beta)=67,5°$	$Vc(\varphi)=\frac{N*\pi*R*Sin(\varphi)}{500}$	Eq. 3
	**Conic Part**	$\varphi_{lim1}<\varphi<\varphi_{lim2}$ $\varphi_{lim1}=(90°-\beta)=67,5°$ $\varphi_{lim2}=132,38°$	$Vc(\varphi)=\frac{N*\pi*R*Sin(\varphi)}{500*Sin(\varphi+\beta)}$	Eq. 4
	**Cylindric part**	$\varphi_{lim2}<\varphi<\varphi_{lim3}$ $\varphi_{lim2}=132.38°$ $\varphi_{lim3}=173°$	$Vc=\frac{N*\pi*D}{1000}=cte$	Eq. 5
R(mm), φ(deg), β(deg), N(rpm), Vc(m/min)				

Tab. 4: Effective grinding speed equations as a function of contact configuration for the CER tool.

The equations in Table 4 allow the graphical representation of the non-linear evolution of the effective grinding speed as a function of the angular position (φ) (Fig. 5). Three spindle speeds currently used in dental milling machines are represented. The tool geometry is discontinuous at the tangency between the conical and cylindrical sections (φlim_2), leading to a discontinuity in $V_c(\varphi)$. A significant increase in $V_c(\varphi)$occurs along the conical section, whereas on the cylindrical section the grinding speed remains constant and independent of the angular position.

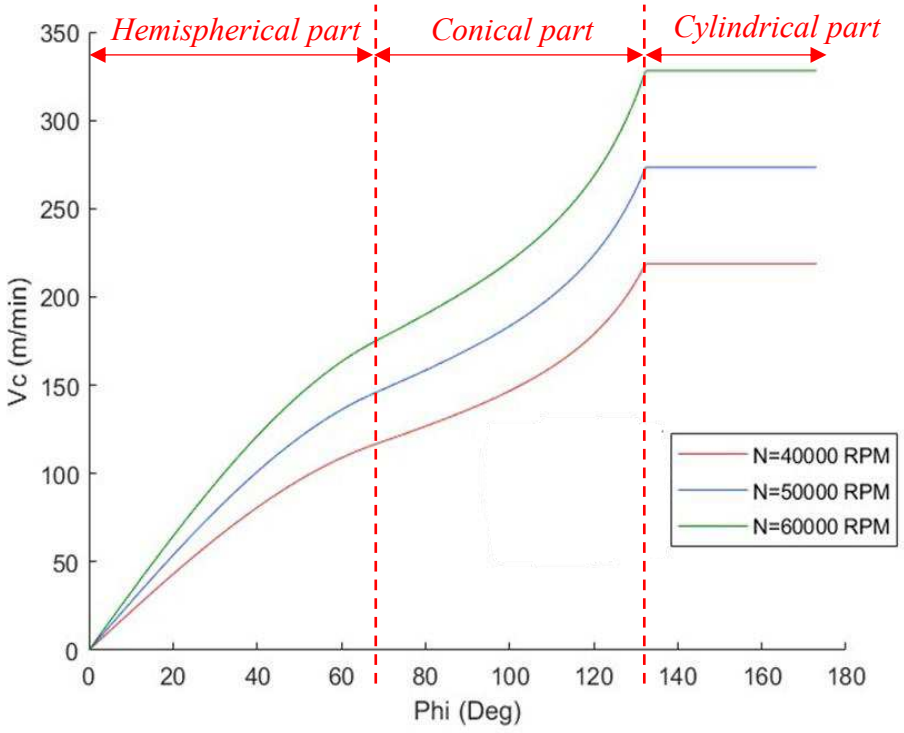


Fig. 5: Vc(φ) trend for the CER bur.

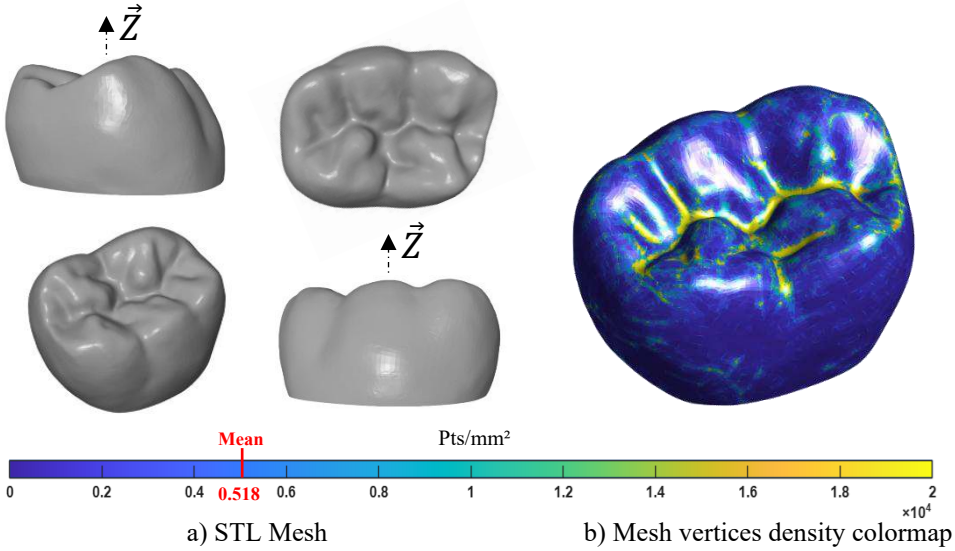
3. Implementation of the models for the manufacturing of a dental crown

The models previously presented were implemented in MATLAB to conduct an analysis of the tool-prosthesis contact during milling.

3.1 Prosthetic shape - CAD model

The geometric model used in this study corresponds to the external surface (extrados) of a dental crown obtained from a chairside clinical case. This prosthesis is representative of the types of crown restorations commonly used in routine clinical practice. The CAD model of the prosthesis is a meshed STL model composed of 53 880 triangular facets and 27 174 vertices, ensuring a detailed discretization of the freeform surface (Fig. 6a). To optimize the size of the STL file, the vertex density is higher in areas with a low radius of curvature. The bottoms of grooves and fossae, therefore, have a higher vertex density (Fig. 6b). Overall, an average density of 0.518 vertice per square millimeter was observed.

In dental CAM software, the prosthesis model is automatically balanced such that its insertion direction of assembly (defined by the prosthesis CAD designer) coincides with the Z-axis direction of the machine-tool. The Z+ direction is oriented externally to the material. This fixed milling direction does not allow the milling of the whole extrados of the prosthesis. To conduct the whole milling of the extrados, the prosthesis is then turned around to the opposite side (180°) with a rotational positioning axis. For the results presented below, only the initial fixed milling direction is considered.



a) STL Mesh b) Mesh vertices density colormap

Fig. 6: STL crown model and its vertices density.

Since the meshes are composed of triangular facets, the geometrical models' implementation is based on this shape discretization. To process, each facet was assigned a unique index *i*, and each vertex with a unique index *j*.

3.2 Tool contact configuration engaged during milling

Θ*i* is defined for each facet *i*, as the angle between the tool axis ($\vec{Z}$) and the surface normal ($\vec{n_i}$) at the contact point A_i (Fig. 7).

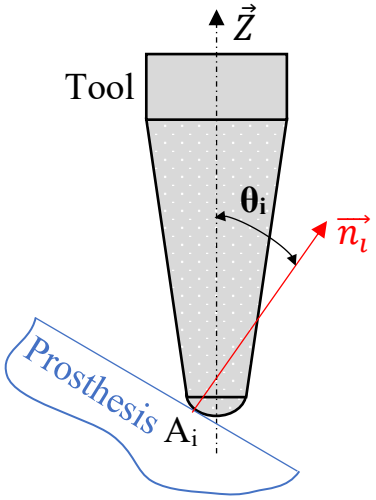


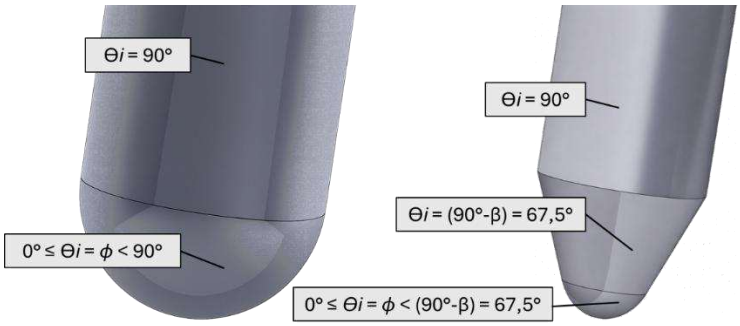
Fig. 7: Tool/prothesis contact schematic and parameters

The components (Xi, Yi, Zi) of the normal $\overrightarrow{n_i}$ of each facet *i* are contained in the STL file. So, the angle Θ*i* is deduce from the normal $\overrightarrow{n_i}$ of the considered facet in the STL file thanks to Eq. 6.

$$\Theta_i = abs\,(cos^{-1}(\overrightarrow{n_i}.\vec{Z})) \qquad \text{Eq. 6}$$

For contact points on the hemispherical tip, the angular position φ coincides with θ_i, such that $\varphi = \theta_i$.

Once the angle Θ*i* known, the tool contact configuration engaged during milling can finally be defined for each facet as shown in figure 8. The hemispherical portion of the tool is engaged when $0° \leq \theta_i < 90°$ for the PM tool and when $0° \leq \theta_i < 67.5°$ for the CER tool. For the CER tool, the conical section is active when $\theta_i = 67.5°$. For both tools, contact occurs on the cylindrical part when $\theta_i = 90°$.



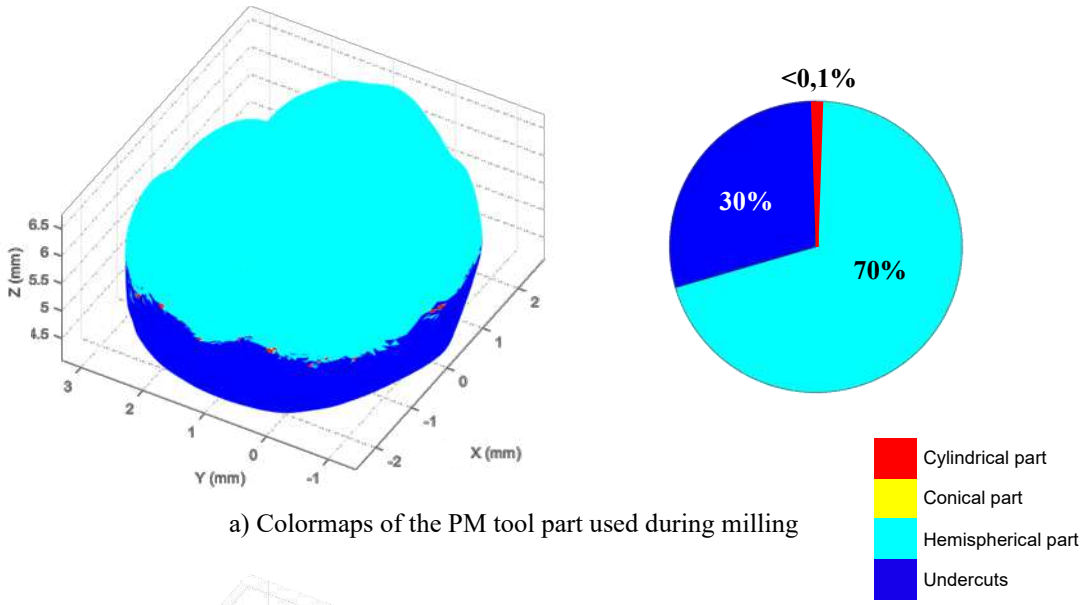
a) PM tool b) CER tool

Fig. 8: Tool/prosthesis contact parameters range

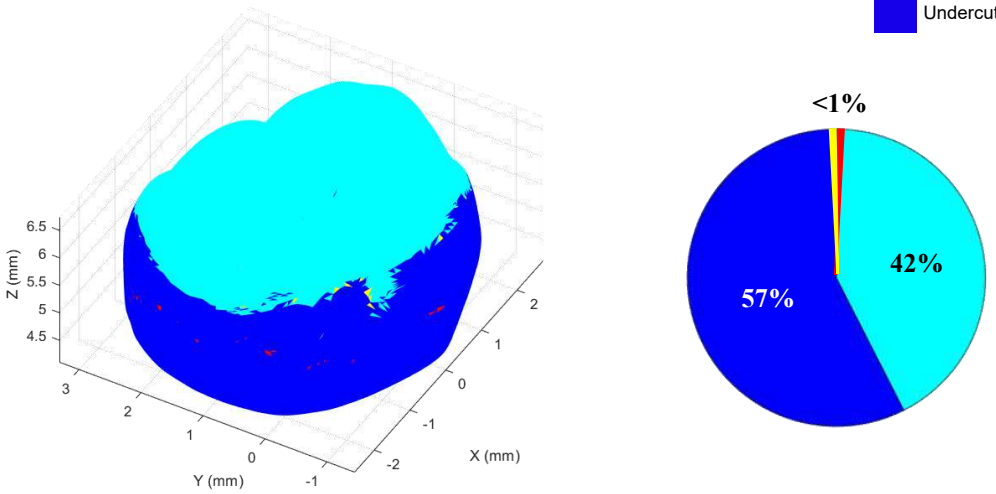
Figure 9 presents the spatial distribution of the tool regions involved in the milling process. For the PM tool, the colormap indicates that the hemispherical part of the tool dominates the milling engagement. The upper portion of the crown surface (occlusal areas in dentistry) is largely covered by the hemispherical part of the tool, while the lower region (peripherical areas in dentistry) corresponds mainly to undercut zones, milled after the 180° turnaround of the prosthesis. 70% of the tool/workpiece interaction occurs on the hemispherical portion, whereas 30% corresponds to undercut regions. The cylindrical part contributes negligibly to the milling process, accounting for less than 0.1% of the total crown surface.

In contrast, the CER tool exhibits a significantly different distribution of engaged zones. The colormap shows a larger spatial extent of undercut areas on the lower portion of the crown. Undercut areas account for approximately 57% of the total surface, while the hemispherical part represents about 42%. The cylindrical and conical parts contribute marginally (<1%). These CER tool parts, therefore, do not contribute significantly to the creation of the finished prosthetic surface.

Overall, the analysis highlights that almost all accessible facets (i.e., those not undercut) of the coronary outer surface are machined using the hemispherical part of the tools (PM tool 30%, CER tool 57% (almost twice)). Indeed, it is very difficult to have facets on the prosthesis with an orientation that exactly matches the orientation of the conical or cylindrical part of the tool. Since the CER tool has a conical section between its cylindrical and hemispherical parts, it generates a smaller hemispherical part, leading to a larger undercut surface. Both tools used almost exclusively the hemispherical part of the tool, resulting in intensive use that causes premature wear.



a) Colormaps of the PM tool part used during milling



b) Colormaps of the CER tool part used during milling

Fig. 9: Colormaps of the tool part used during milling.

3.2.1 Grinding speeds analysis

The grinding speed $V_{C_i}$was computed for each facet i. For contacts on the hemispherical portion of the tool, equation 3 was applied with $\varphi = \theta_i$. For contacts on the cylindrical flank, equation 4 was directly implemented, using D as the cylindrical tool diameter. For the conical section, the calculation of V_{C_i} requires determining the position of the contact point A_i over the cone. However, this information is not readily available, as all facets in contact with the conical section share the same surface normal. To simplify the implementation, the effective grinding speed on the conical section was approximated by its mean value over the cone (Eq. 7). The impact of this approximation is expected to be negligible, as the conical region is engaged in less than 0.1% of the grinding process (§3.2).

$$Vc_i = \frac{\pi * N * (D + 2R * cos(\beta))}{2000} \qquad \text{Eq. 7}$$

Figure 10 presents the spatial distribution of the tool grinding speeds involved during the milling process. The three most commonly used spindle speeds used with the dental milling machine were retained [18-19].

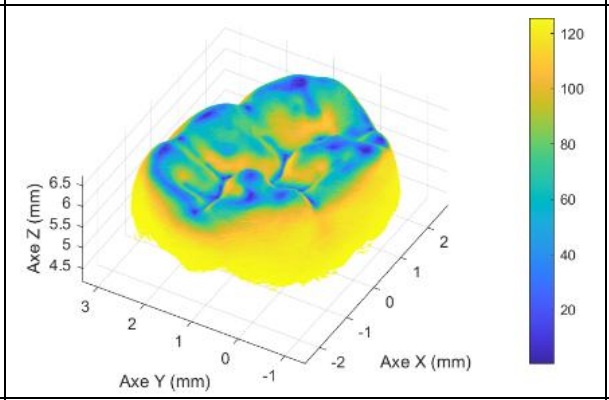
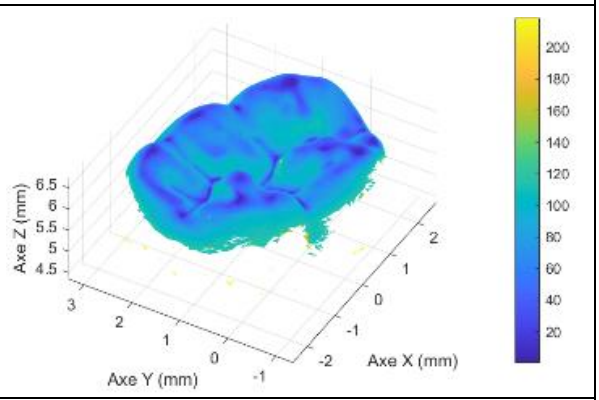
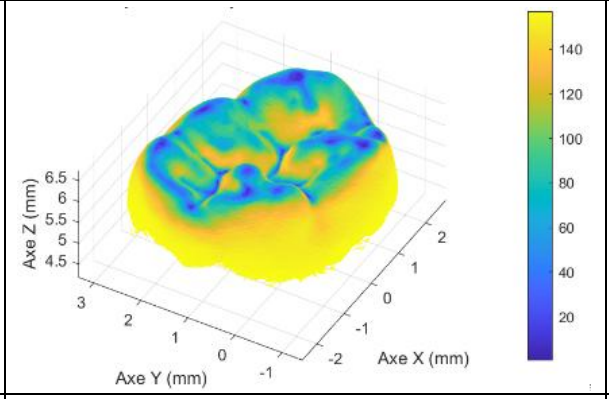
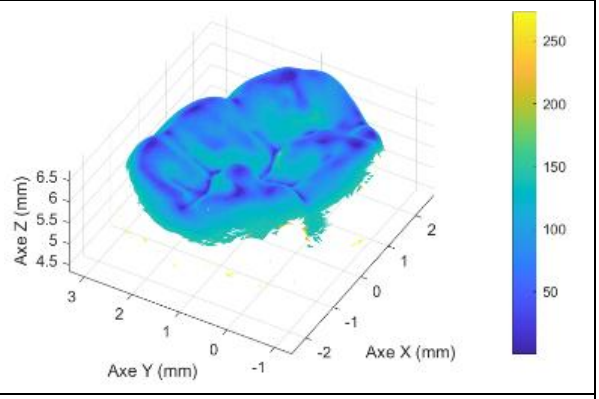
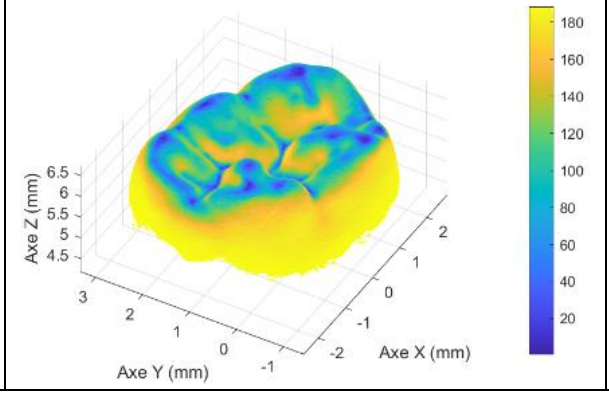
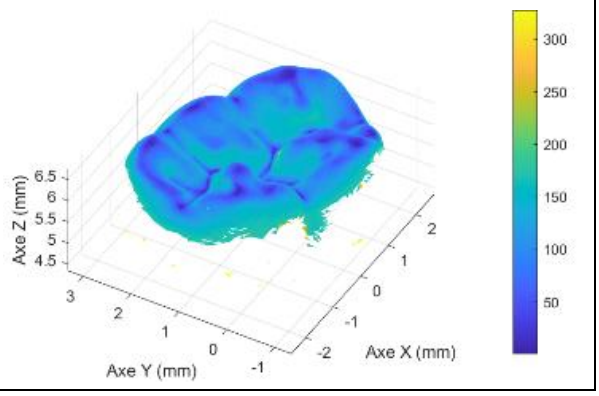
Vci (m/min)	PM	CER
40 000 RPM		
50 000 RPM		
60 000 RPM		

Fig. 10: Colormaps of effective grinding speeds at different spindle speeds.

Under the simulated conditions, the effective grinding speeds vary between 0 and 330 m/min. Two main sources of variation in the effective grinding speed have been identified: (1) variations in tool geometry, and (2) differences in spindle rotational speeds across milling machines.

Regarding differences in tool geometry, at a given spindle speed, the CER tool attains a maximum effective grinding speed approximately 57% higher than that of the PM tool. This difference arises from its larger cylindrical section diameter ($D_{CER} = 1.74$ mm vs $D_{PM} = 1$mm). However, the

cylindrical part of the CER tool is involved in machining only a very limited number of facets, representing less than 1% of the total coronal surface area (see §3.2). Over nearly the entire accessible coronal surface (i.e. excluding undercuts and the small fraction of facets machined by the cylindrical and/or conical regions) both tools primarily engage their hemispherical parts (see §3.2). As this part has an identical diameter for both tools (1 mm), the resulting effective grinding speeds are equivalent when machining with the hemispherical part.

Variations in spindle speed result in variations in the effective grinding speed of up to 33%. These variations in effective grinding speed affect surface integrity. As a result, two identical prostheses, machined on two different CNC machines, perform differently in terms of their expected functionality.

Regardless of the tool used, the lowest effective grinding speeds are achieved on the occlusal surface (cusp tips), where the facets are machined with the tip of the tool. The highest effective grinding speeds, on the other hand, occur on the peripheral surfaces, where the facets are abraded with the flank of the tool. As a result, surface integrity will be different according to the location on the milled crown. Areas milled with the tip of the tool (i.e. lowest grinding speeds) will exhibit lower surface roughness, an isotropic surface topography, and an accelerated tool wear leading to a lapping phenomenon [20-21]. On the other hand, areas milled with the flank of the tool (i.e. highest grinding speeds) will exhibit higher surface roughness and anisotropic surface topography [22].

3.2.2 Curvature analysis for tool tip accessibility

To complete the analysis of the tool-workpiece contact, a curvature-based analysis of the prosthesis geometry is conducted to identify regions that are inaccessible to the tool and therefore not machinable.

The principal curvature radii (k_1 and k_2) were evaluated over the entire previous CAD surface (Fig.6). Then, the Gaussian (K) and mean (H) curvatures were computed [23]. K and H curvatures were calculated as follows: (Eqs. 8, 9).

$$K = k_1 \text{x } k_2 \qquad \text{Eq. 8}$$

$$H = \frac{1}{2}(k_1 \text{x } k_2) \qquad \text{Eq. 9}$$

Following the classification proposed by Besl [24], the signs of the Gaussian (K) and mean (H) curvatures were then used to identify the fundamental surface types, allowing each area of the prothesis geometry to be categorized into eight distinct surface classes (Fig. 11). The considered

classes include convex configurations (peak, ridge), concave configurations (pit, valley), saddle configurations (saddle ridge, saddle valley), and transitional cases (flat surface and minimal surface). This approach enables a fine-scale topological characterization of the surface beyond global curvature descriptors.

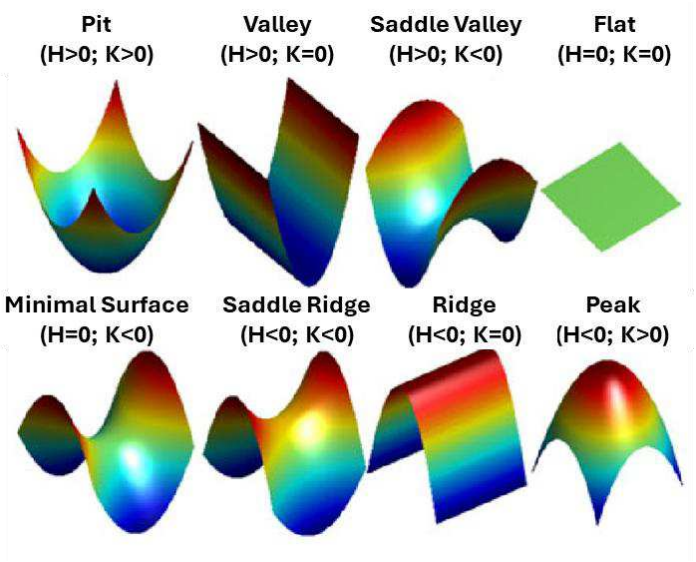


Fig. 11: Representations of basic types of surfaces based on signs of Gaussian and mean curvatures [24]

Once the principal curvature radii and the Gaussian and mean curvatures were evaluated at each vertex *j*, the basic types of surfaces were identified for each vertex of the mesh.

Subsequently, the regions inaccessible to the milling tool were identified. Two geometric conditions were required to classify an area as unreachable. First, the local surface type had to belong to one of the five concave categories, namely pit, valley, minimal surface, saddle ridge, or saddle valley, according to the previous curvature-based classification. Second, at least one of the two principal curvature absolute radii value ($|k_{1j}|$ or $|k_{2j}|$) had to be smaller than the radius of the ball-end milling tool ($k_{1j} < R$ or $k_{2j} < R$). When these conditions are satisfied, the local surface curvature exceeds the tool curvature, preventing full contact between the tool and the surface and thereby rendering the region non-machinable under three-axis constraints.

The analyzed crown surface was decomposed using the basic types of curvature (fig. 2). Each vertex was assigned to one of eight canonical surface basic types. Figure 12 shows the spatial distribution of the basic types of curvature.

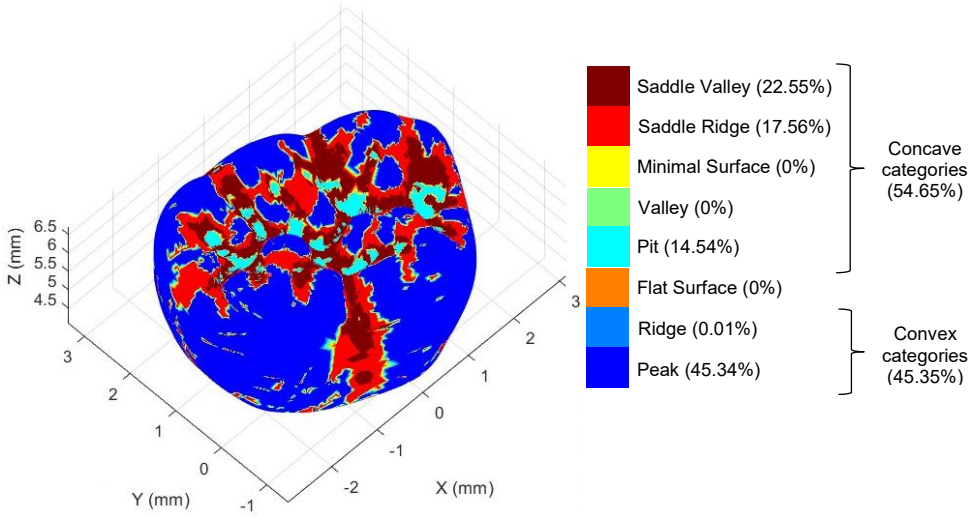
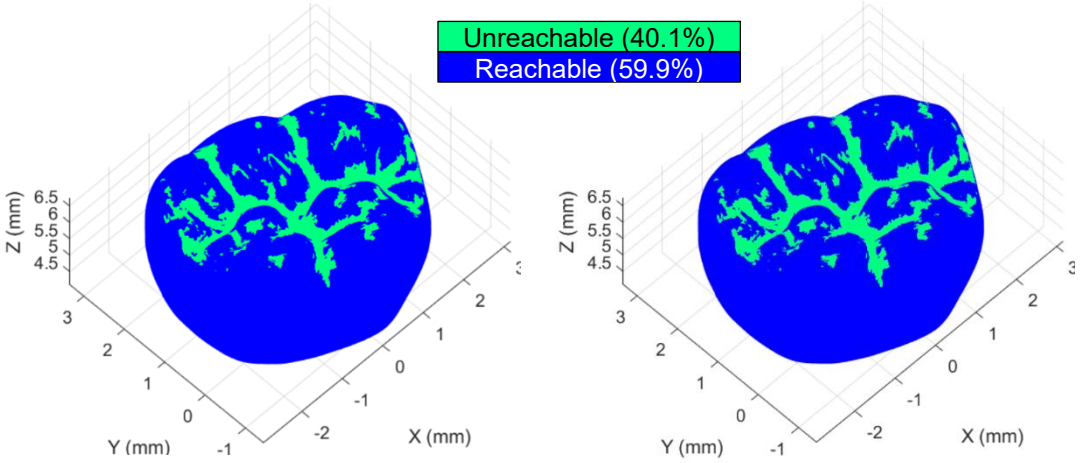


Figure 12. The eight basic types of surfaces identified on the CAD crown colormap.

The results reveal a strongly heterogeneous curvature organization. The peak category is predominant, accounting for 45.34% of the vertices. Saddle configurations are also highly represented, with saddle valley and saddle ridge contributing 22.55% and 17.56%, respectively. The saddle regions correspond to areas where the principal curvatures have opposite signs ($k_1 \cdot k_2 < 0$), indicating high curvature asymmetry. The pit regions, representing 14.54% of the surface, are more localized and scattered, representing isolated of negative Gaussian curvature. In contrast, the ridge category is negligible (0.01%), while valley, flat surface, and minimal surface categories are absent. When grouped, convex regions (peak and ridge) account for 45.35% of the vertices, whereas concave and saddle-related regions represent 54.65%. These results indicate that the crown surface is dominated by non-zero Gaussian curvature, with a slight predominance of negative or mixed curvature states.

Based on the two accessibility conditions defined previously, tool accessibility is computed and mapped in Fig. 13; It presents a comparative reachability analysis of a complex three-dimensional crown geometry using the two different tools (PM and CER).



a) PM tool accessibility b) CER tool accessibility

Figure 13. Reachable and unreachable areas applied to the CAD crown colormap.

The two colormaps are identical because the part of the tool engaged during machining is the hemispherical tip for both tools (§3.2). Moreover, both tools have the same diameter (D = 1 mm).

So, in both cases, the spatial distribution of accessible and inaccessible areas remains similar, with 59.9% of the surface classified as reachable and 40.1% as unreachable. The inaccessible regions, corresponding to the deepest areas of the grooves, exhibit a branching, vein-like structure characteristic of geometrically constrained areas such as concavities, cavities, and regions of high negative curvature. These patterns indicate that the primary limitations arise from geometric factors, including self-shadowing effects and restricted tool approach directions, rather than from the specific tool geometry. Consequently, enhancing reachability would likely require more advanced strategies, such as multi-axis reorientation, multi-tool approaches. Overall, the results highlight that, for highly complex geometries, accessibility is predominantly governed by intrinsic shape characteristics linked to the tool geometry.

The curvature analysis reveals a clear multi-scale organization of the molar surface. At the global scale, convex regions form a continuous envelope that reflects the overall rounded morphology of the tooth crown. This predominance of convexity is consistent with the anatomical role of molars, which are adapted to withstand and distribute compressive loads during mastication. Superimposed on this global convex geometry is a structured network of saddle regions corresponding to the characteristic grooves of molar anatomy. These interconnected saddle configurations are distributed across the occlusal surface, delineating cusp boundaries and contributing to the guidance and fragmentation of food during chewing.

When accessibility results are considered alongside the curvature analysis, a strong relationship emerges between geometric complexity and machinability. The inaccessible regions are predominantly concentrated within the deepest occlusal grooves and fossae, which are characterized by saddle and pit curvatures. In contrast, the convex cusp regions, representing approximately 59.9% of the surface, remain largely accessible. The remaining 40.1% corresponds mainly to anatomically significant concave and hyperbolic features that are difficult or impossible to machine due to geometric constraints such and limited tool approach directions.

From an anatomical and functional perspective, these inaccessible regions are of particular importance because they coincide with the structures responsible for maintaining the occlusal relief of the molar. Grooves and fossae not only separate cusps but also guide food flow, promote efficient food fragmentation, and contribute to the distribution of occlusal contacts during mastication. Consequently, the incomplete reproduction or loss of these features may alter the natural chewing mechanism, reduce masticatory efficiency, and modify contact patterns between opposing teeth. The inaccessible regions therefore represent more than simple manufacturing limitations; they correspond to potential losses of functional anatomy.

Overall, the results demonstrate that accessibility constraints are concentrated in the very features that contribute most to the local geometric complexity and biomechanical performance of the tooth. This finding highlights the critical interplay between morphology, function, and manufacturability, and emphasizes the need for advanced machining strategies, such as multi-axis tool orientations or multi-tool approaches, to preserve anatomically and functionally relevant surface characteristics.

4. Conclusion

This study provided a comprehensive geometrical and kinematic analysis of tool-workpiece interactions during three-axis milling of dental prostheses. By combining curvature-based surface characterization with analytical modeling of tool geometry and contact conditions, it was possible to accurately describe the spatial variability of effective grinding speed, surface integrity, and machining accessibility across a complex crown geometry.

The results demonstrate that, regardless of the tool geometry, the hemispherical part of the bur is predominantly engaged during machining. This leads to highly non-uniform grinding conditions, with significant spatial variations in effective grinding speed driven by local surface orientation. In particular, low grinding speeds are systematically observed at cusp tips (local protrusion in the upper surface of the prosthesis), while higher speeds occur along peripheral regions. These

variations are expected to induce heterogeneous surface integrity, including differences in roughness, topography, and tool wear mechanisms across the prosthesis.

The comparison between the two investigated tools highlights those geometric differences, such as the presence of a conical section, have a limited practical impact on machining conditions. Indeed, these additional tool features are only marginally involved in the grinding process. Instead, the effective grinding behavior is largely governed by the common hemispherical tip geometry, emphasizing its critical role in tool performance and wear.

Furthermore, the curvature-based accessibility analysis revealed that approximately 40% of the prosthetic surface remains unreachable under three-axis machining constraints. These inaccessible regions are primarily associated with concave and highly curved anatomical features, such as grooves and fossae. This limitation is intrinsic to the combination of tool geometry and fixed tool orientation and cannot be overcome without modifying the machining strategy.

Overall, this work highlights the strong coupling between prosthesis geometry, tool design, and machining kinematics in dental CAD/CAM processes. The proposed modeling framework provides valuable insights for understanding machining-induced variability and could support the optimization of tool design, spindle speed selection, and toolpath strategies. In particular, the results suggest that improving surface quality and accessibility would require advanced approaches, such as multi-axis machining, adaptive tool orientation, or multi-tool strategies. These perspectives open promising directions for enhancing the accuracy, durability, and functional performance of dental prostheses manufactured by CAD/CAM technologies.

Statements & Declarations

Funding

The authors declare that no funds, grants, or other support were received during the preparation of this manuscript.

Competing Interests

The authors have no relevant financial or non-financial interests to disclose.

Author Contributions

The first draft of the manuscript was written by N. Lebon, and L. Tapie provided comments on previous versions of the manuscript. All authors read and approved the final manuscript.

References

[1] Kurbad A (2017) A new milling machine for computer-aided, in-office restorations. Int J Comput Dent 20(2):201-213. PMID: 28630960

[2] Lebon N, Tapie L, Vennat E, Mawussi B, Attal JP (2014) Influence of the tool-material couple on the dental CAD/CAM prosthetic roughness. JCM 2014, Toulouse, France. doi: 10.1016/j.prosdent.2014.12.021

[3] Chen T, Shi Z (2008) A tool path generation strategy for three-axis ball-end milling of free-form surfaces. J Mater Process Technol 208(1-3):259-263. doi.org/10.1016/j.jmatprotec.2007.12.142

[4] Aurich JC, Engmann J, Schueler GM, Haberland R (2009) Micro grinding tool for manufacture of complex structures in brittle materials. CIRP annals 58(1):311-314. doi.org/10.1016/j.cirp.2009.03.049

[5] Pratap A, Patra K, Dyakonov AA (2016) Manufacturing miniature products by micro-grinding: a review. Procedia Eng. 150:969-974. doi.org/10.1016/j.proeng.2016.07.072

[6] Setti D, Arrabiyeh PA, Kirsch B, Heintz M, Aurich JC (2020) Analytical and experimental investigations on the mechanisms of surface generation in micro grinding. Int J Mach Tools Manuf 149:103489. doi.org/10.1016/j.ijmachtools.2019.103489

[7] Cheng J, Wang C, Wen X, Gong Y (2014) Modeling and experimental study on micro-fracture behavior and restraining technology in micro-grinding of glass. Int J Mach Tools Manuf 85:36-48. doi.org/10.1007/s12206-017-0629-8

[8] Li W, Ren Y, Li C, Li Z, Li M (2020) Investigation of machining and wear performance of various diamond micro-grinding tools. Int J Adv Manuf Technol 106(3):921-935. doi.org/10.1007/s00170-019-04610-4

[9] Lebon N, Tapie L (2022). Surface integrity of pre-sintered ceramics and composites used for dental prostheses after CAD/CAM abrasive milling. Procedia CIRP 108:252-257. doi.org/10.1016/j.procir.2022.03.044.

[10] Batham H, Patel D, Banerjee T (2022) A review on fabrication, grinding performance and failure of micro-grinding tools. Mat Today 66:3870-3877. doi.org/10.1016/j.matpr.2022.06.304

[11] Srinivas MS, Sangeeth P, Venkaiah N, Sankar, MR (2023) State of the art on tool wear characterization in micro-milling. Mat Today doi.org/10.1016/j.matpr.2023.07.019

[12] Feng J, Kim BS, Shih A, Ni J (2009) Tool wear monitoring for micro-end grinding of ceramic materials. J Mater Process Technol 209(11):5110-5116. doi.org/10.1016/j.jmatprotec.2009.02.009

[13] Denkena B, Friemuth, T, Reichstein M, Tönshoff HK (2003) Potentials of different process kinematics in micro grinding. CIRP Annals 52(1), 463-466. doi.org/10.1016/S0007-8506(07)60626-X

[14] Li W, Long C, Deng Z, Guo X, Ren Y, Lin Q, Shen B (2024) Machining performance and wear mechanism of CVD diamond-coated micro-grinding tools in micro-grinding of fused silica. J Manuf Process 131:1168-1178. doi.org/10.1016/j.jmapro.2024.09.037

[15] Zhou L, Lin YJ (2001) An effective global gouge detection in tool-path planning for freeform surface machining. Int J Adv Manuf Technol 18(7):461-473. doi.org/10.1007/s0017010180461

[16] Pacquet W, Tapie L, Mawussi B, Boitelle P (2023) Volumetric and dimensional accuracy assessment of CAD-CAM–manufactured dental prostheses from different materials. J Prosthet Dent 129(1):150-159. doi.org/10.1016/j.prosdent.2021.05.024

[17] Engin S, Altintas Y (2001) Mechanics and dynamics of general milling cutters.: Part I: helical end mills. Int J Mach Tools Manuf 41(15):2195-2212. doi.org/10.1016/S0890-6955(01)00045-1

[18] Lebon N, Tapie L, Duret F, Attal JP (2016) Understanding dental CAD/CAM for restorations: dental milling machines from a mechanical engineering viewpoint. Part A: Chairside milling machines. Inter J Comput Dent 19(1):45-65. PMID: 27027102

[19] Lebon N, Tapie L, Duret F, Attal JP (2016) Understanding dental CAD/CAM for restorations - dental milling machines from a mechanical engineering viewpoint Part B: Labside milling machines, Inter J Comput Dent 19(2):115-134, PMID:27274561

[20] Iliescu AA, Perlea P, Iliescu MG, Gheorghiu IM (2018) Milling machines tools used in cad-cam technology of dental prostheses. Rom J Oral Rehabil 10(4).

[21] Lebon N, Tapie L (2022) Surface Integrity of Pre-sintered Ceramics and Composites Used for Dental Prostheses After CAD/CAM Abrasive Milling, Procedia CIRP 108(8)252–257. doi.org/10.1016/j.procir.2022.03.044

[22] Lebon N, Tapie L, Vennat E (2020) Influence of Milling Tool and Prosthetic Materials on Roughness of the Dental CAD CAM Prostheses. End Milling Mode. Appl Sci 7:2238-2252. doi.org/10.3390/app10072238

[23] Feng X, Xia K, Tong Y, Wei GW (2012) Geometric modeling of subcellular structures, organelles, and multiprotein complexes. Int J Numer Methods Biomed Eng 28(12):1198-1223. doi.org/10.1002/cnm.2532

[24] Besl PJ (2012) Surfaces in range image understanding. Springer Science & Business Media, Berlin